

# Early neural activity changes associated with stimulus detection during visual conscious perception

Aya Khalaf<sup>1,2</sup>, Sharif I. Kronemer<sup>1,3</sup>, Kate Christison-Lagay<sup>1</sup>, Hunki Kwon<sup>1</sup>, Jiajia Li<sup>1,4</sup>, Kun Wu<sup>6</sup>, Hal Blumenfeld<sup>1,5,6,\*</sup>

<sup>1</sup>Department of Neurology, Yale University School of Medicine, 333 Cedar Street, New Haven, CT 06520, United States,

<sup>2</sup>Biomedical Engineering and Systems, Faculty of Engineering, Cairo University, Giza 12613, Egypt,

<sup>3</sup>Interdepartmental Neuroscience Program, Yale University School of Medicine, 333 Cedar Street, New Haven, CT 06520, United States,

<sup>4</sup>School of Information & Control Engineering, Xian University of Architecture & Technology, Xi'an 710055, China,

<sup>5</sup>Department of Neuroscience, Yale University School of Medicine, 333 Cedar Street, New Haven, CT 06520, United States,

<sup>6</sup>Department of Neurosurgery, Yale University School of Medicine, 333 Cedar Street, New Haven, CT 06520, United States

\*Corresponding author: Departments of Neurology, Neuroscience, and Neurosurgery, Yale University School of Medicine, 333 Cedar Street, New Haven, CT 06520-8018, United States. Email: hal.blumenfeld@yale.edu

The earliest cortical neural signals following consciously perceived visual stimuli in humans are poorly understood. Using intracranial electroencephalography, we investigated neural activity changes associated with the earliest stages of stimulus detection during visual conscious perception. Participants ( $N = 10$ ; 1,693 electrode contacts) completed a continuous performance task where subjects were asked to press a button when they saw a target letter among a series of nontargets. Broadband gamma power (40–115 Hz) was analyzed as marker of cortical population neural activity. Regardless of target or nontarget letter type, we observed early gamma power changes within 30–180 ms from stimulus onset in a network including increases in bilateral occipital, fusiform, frontal (including frontal eye fields), and medial temporal cortex; increases in left lateral parietal–temporal cortex; and decreases in the right anterior medial occipital cortex. No significant differences were observed between target and nontarget stimuli until  $>180$  ms post-stimulus, when we saw greater gamma power increases in left motor and premotor areas, suggesting a possible role in perceptual decision-making and/or motor responses with the right hand. The early gamma power findings support a broadly distributed cortical visual detection network that is engaged at early times tens of milliseconds after signal transduction from the retina.

**Key words:** broadband gamma; consciousness; detection; intracranial EEG; visual perception.

## Introduction

With myriad sensory inputs, the nervous system requires a mechanism to identify the most salient signals for additional processing and event emergence in the context of conscious perception. Broadly, this process is known as *detection*, which acts in the earliest stages of sensory processing to rapidly identify target inputs and guides the processing of the most relevant sensory stimuli in higher-order sensory and association cortices for subsequent conscious report (Thompson and Schall 2000; Libedinsky and Livingstone 2011; Herman et al. 2019). Based on recent experimental findings, we hypothesized that detection of stimuli forms the crucial first step in the multistep sequence of overlapping cortical and subcortical mechanisms enabling conscious perception (Blumenfeld 2021). In tasks requiring attentional vigilance, such as stimulus identification and decision-making, all or nearly all stimuli are assumed to be consciously perceived. In these tasks, rapid stimulus detection is necessary for subsequent steps of conscious perception and action. Investigating whole-brain signals in humans at high time

resolution would be highly beneficial to better identify the networks involved in the early detection step of conscious perception.

Because speedy detection is essential for timely decision-making and behavior, the stimulus detection network should be active beginning at the earliest times after signal transduction from the sensory organs. For example, several studies showed that signal latency between the retina and primary visual cortex can be as early as 50 ms or less, corresponding to the arrival of signals to the visual detection network (Schmolesky et al. 1998; Deco and Lee 2004; Meeren et al. 2008; Kirchner et al. 2009; Shigihara et al. 2016; Kwon et al. 2021). Non-sensory cortex also contributes to detection because of long-range cortico-cortical and thalamo-cortical projections allowing for rapid access to sensory signals in association cortices. Several human and nonhuman primate studies identify the prefrontal cortex as a possible contributor in early signal processing. In nonhuman primate studies, the frontal eye fields (FEFs) were found to be involved in stimulus detection within 100 ms from stimulus onset and even earlier, showing

visual-evoked response that peaked ahead of V2 and V4 (Schmolsky et al. 1998; Thompson and Schall 1999, 2000; Bichot and Schall 2002; Gregoriou et al. 2009; Libedinsky and Livingstone 2011; Bollimunta et al. 2018). Human studies found similar results with early FEF activity within 100 ms from stimulus onset and even as early as 50 ms post-stimulus (Blanke et al. 1999; Foxe and Simpson 2002; Muggleton et al. 2003; O'Shea et al. 2004). Other human studies showed increased activity in FEF nearly as fast as the primary visual cortex. It was found that FEF is activated within 24 ms post auditory stimulus onset and 45 ms post visual stimulus onset (Kirchner et al. 2009), while in another investigation, FEF showed increased activity within 50 ms post-stimulus (Kwon et al. 2021). Beyond the FEF, a functional magnetic resonance imaging (fMRI) study revealed that the inferior frontal cortex plays a critical role in stimulus detection (Weilhammer et al. 2021).

Other regions have also been linked with detection, particularly the parietal cortex as a top-down attention feedback structure that communicates with the sensory cortices to modulate the neuronal signals to promote higher-order processing (Critchley 1962; Corbetta and Shulman 2002; Saalmann et al. 2007; Gregoriou et al. 2009; Bisley and Goldberg 2010). This is corroborated by clinical instance of spatial neglect resulting from parietal cortex impairment that can produce the inability to attend to sensory inputs from a neglected field (Parton et al. 2004). Other regions linked to detection include medial temporal lobe and medial frontal cortex (Wang et al. 2018). Together, these findings reveal that the detection network possibly engages a broad set of sensory and association regions, both in cortical and subcortical structures, all with early signaling properties. However, many of the nuances of the physiology underlying detection remain unknown.

In the current investigation, we study the spatiotemporal dynamics of cortical networks associated with visual stimulus detection using a continuous performance task (CPT) and intracranial EEG (icEEG) recordings. Despite the limitations of heterogeneous coverage and the confounds of a patient population, icEEG is ideal for examining the human detection network because of its anatomical precision, high temporal resolution, and high signal-to-noise ratio compared to other human brain imaging modalities, all of which are necessary to capture small, rapid, and transient electrophysiology (Parvizi and Kastner 2018). The analyses we implemented focused on investigating the spatiotemporal dynamics of broadband gamma power (40–115 Hz), which have been shown to reflect the activity of the local neuronal population (Mukamel et al. 2005; Manning et al. 2009; Ray and Maunsell 2011). Such analyses revealed a broad set of regions involved in stimulus detection including bilateral visual, bilateral prefrontal, bilateral medial temporal cortex, and left lateral parietal-temporal cortex.

## Materials and methods

### Participants

Ten right-handed adult subjects (females = 6; mean age = 37, range 23–54 years old) undergoing craniotomy with intracranial electrodes for seizure monitoring were recruited from the Yale Comprehensive Epilepsy Program (Table 1). Subjects participated in the study following written informed consent. All research procedures were approved by the local institutional review board (IRB) at Yale University.

The implanted intracranial electrodes included subdural grids, strips, and depth electrodes. Electrode type, number, and placement were determined by the clinical team overseeing each case. Participants were implanted with on average 196 electrodes yielding a total of 1,957 intracranial electrode contacts across all subjects. Through visual inspection of co-registered structural MRI and whole-brain computed tomography (CT) images, a total of 264 electrodes were excluded across all subjects due to localization in white matter. The remaining 1,693 electrodes were located in gray matter and bilaterally distributed across cortical surface and depth sites (Fig. 1B).

### Intracranial EEG data acquisition

The icEEG data were recorded with Natus NeuroLink/Braintronics amplifier and pruned using Natus NeuroWorks software ([www.neuro.natus.com](http://www.neuro.natus.com)). EEG data were sampled at 1,024 Hz and filtered with an analog bandpass filter with corner frequencies of 0.1 and 400 Hz. The clinical team selected the reference electrode for each participant that best reduced the visible EEG artifacts (Table 1). The data of one participant were originally sampled at 256 Hz. To unify the sampling frequency across subjects, the data of that subject were oversampled using the resample function in MATLAB R2019a ([www.mathworks.com](http://www.mathworks.com)) to match the 1,024 Hz sampling rate of all participants.

To ensure proper synchronization between task event times and the corresponding EEG recordings, transistor-transistor logic (TTL) pulses of varying durations were initiated by the experimental laptop at the onset of task events (button presses, letter presentations, and rest/active phase onsets). The duration of the TTL pulses differed according to the event type to allow differentiation between the events. These TTL pulses were generated by an Arduino Uno (R3; Smart Projects, model A000066) and delivered directly to an open recording channel in the icEEG recording system. The TTL pulses in this channel were used to extract data corresponding to salient task events.

### Continuous performance task

The CPT is a commonly used paradigm to study mechanisms of attention and perception in healthy and clinical populations (Beck et al. 1956; Riccio et al. 2002; Killory et al. 2011). In this study, participants were asked to

**Table 1.** Patient demographic information, number of intracranial electrode contacts, and reference electrode locations.

Participant	Age (years)	Gender	Handedness	Number of electrodes	Reference electrode location
1	31	M	Right	286	Right lateral frontal ISS
2	32	F	Right	197	Right inferior frontal ISS
3	54	F	Right	114	Left lateral parietal ISS
4	48	F	Right	241	Right lateral parietal ISS
5	37	F	Right	133	Right lateral frontal SS
6	31	F	Right	172	Right superior frontal SS
7	23	M	Right	238	Right lateral frontal ISS
8	35	M	Right	240	Right superior frontal ISS
9	52	F	Right	204	Left lateral frontal ISS
10	25	M	Right	132	Left lateral parietal ISS

ISS, inverted subdural strip; SS, skull screw.

complete a CPT paradigm coded in Python, run with PsychoPy v1.83 ([www.psychopy.org](http://www.psychopy.org)), and presented on a laptop equipped with an NVIDIA GeForce graphics card and 15.6-inch screen display.

The CPT paradigm was composed of alternating blocks of 32-s active task and 32-s rest phases (Fig. 1A). During the active task phase, random white capital English letters (A, B, C, D, E, F, G, H, I, L, M, N, O, T, Y, X, and Z; visual angle = 1.75°) were presented in random order at the center of the screen on a black background. A total of 32 letters were presented during blocks of the active task phase. The probability of presenting the target letter X within each block was 23.5%. Letters were presented at a rate of 1 Hz and displayed for 250 ms followed by a 750-ms interstimulus interval blank period (black screen) before the presentation of the next letter (or the onset of the rest phase). Participants were instructed to maintain fixation at the center of the screen and immediately respond with a right thumb button press whenever the target letter X appeared. Participants used a response box (In-Line Trainer, Current Designs, Inc., SKU OTR-1x4-L) to deliver their task responses. During the rest phase, participants were instructed to passively view a white fixation cross (visual angle = 1.21°) displayed at the center of the screen on a black background.

A single run of the CPT task consisted of 10 blocks of alternating fixation (rest) blocks and active task blocks (5 fixation blocks and 5 active task blocks). The number of runs completed by each participant varied depending on patient in-house availability, duration of stay, and willingness to participate in the study. A total of 63 runs were completed by the 10 participants.

Participants performed the CPT task in their hospital bed. The testing laptop was placed 85 cm away from the participant on a bedside table. To ensure the same ambient lighting conditions across participants and sessions, window blinds were drawn, and lights were switched off during testing.

### Epoch segmentation and preprocessing

The event epochs corresponding with letter stimuli presentation were extracted. Each epoch was 4 s in duration and centered at the onset of each letter

stimulus. The first 3 letters of each active task block were excluded from the analysis due to a transient signal increase corresponding with the task onset (Li et al. 2019). Letter epochs containing clinical or subclinical epileptic events determined by visual inspection were excluded from the analysis. The remaining epochs were processed using a 4-staged artifact rejection pipeline adopted from Herman et al. (2019) and Li et al. (2019). First, for each epoch, the power spectrum of each electrode was estimated using Welch's power spectral density method in MATLAB R2019a. To remove trials with high frequency noise, epochs showing peaks with a topographical prominence greater than 200  $\mu\text{V}/\text{Hz}$  at frequencies greater than 10 Hz were rejected. Next, to detect disconnected or loose electrodes, the mean square error (MSE) was calculated relative to zero for each electrode within each epoch. Epochs with MSE less than 200  $\mu\text{V}^2$  were excluded. Third, the MSE value for each electrode within each epoch was calculated relative to its mean voltage time course averaged within-subject. Epochs that deviated from the mean time course by an MSE > 3,000  $\mu\text{V}^2$  were excluded. If more than 20% of the epochs for a subject were marked for exclusion according to this criterion, only the top 20% noisiest epochs would be excluded to balance considerations of noisy data and sample size, as in prior work from our group (Herman et al. 2019; Li et al. 2019). Finally, for each electrode, the standard deviation (SD) was calculated across epochs. Epochs that reaching voltages greater than 5 SD were excluded. Across all subjects, this in-house preprocessing pipeline rejected 20% of the letter epochs.

After all letter epochs were passed through the above rejection procedure, the remaining epochs were categorized into specific task event types. Two categories of trials were considered for further analysis in the current study: (i) target letter X trials when the participant successfully responded with a right thumb button press (X-Press trials) and (ii) nontarget letter trials (all non-X stimuli) when the participant correctly withheld a button response (NonX-NoPress trials). The average hit rate (percentage of correctly identified target trials) across all participants was  $95.6\% \pm 3.4\%$  (mean  $\pm$  SD), while the average false alarm rate (percentage of nontarget trials identified as target trials) was  $0.8\% \pm 0.9\%$ . Average

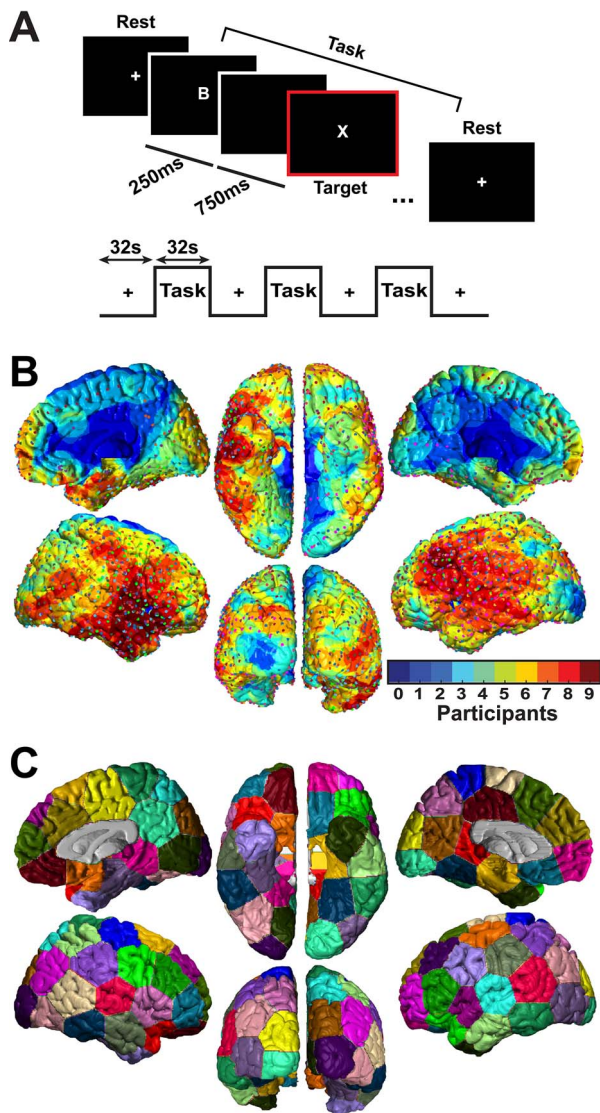


**Fig. 1.** CPT, intracranial electrode distribution, and parcellation map. A) CPT task consists of alternating rest and active task phases, each lasting for 32 s. During the active task phase, 32 English letters were presented for 250 ms at a rate of 1 Hz. Participants were instructed to press the right-thumb button whenever a target stimulus (X letter) is presented. B) Density map of 1,693 intracranial electrodes implanted in 10 participants is displayed on a common MNI-space brain surface. Signals from each electrode are represented as a spherical space of 15 mm radius measured from the electrode central location. The map shows the number of participants contributing to signal analysis at each vertex on the brain surface model. The highest electrode coverage was 9 participants at some brain regions. C) An example of the 120-Parcel bilateral parcellation map generated using K-means clustering algorithm. To ensure statistical findings were invariant to changes in parcellation map construction and parcel locations, 100 such parcellation maps were constructed and statistical results were aggregated over the findings from each map.

response time of X-Press trials across participants was  $484 \text{ ms} \pm 51 \text{ ms}$ .

### Broadband z-score gamma power calculation

In previous studies, local broadband gamma activity increases, along with delta–theta (1–8 Hz) activity increases and alpha–beta (8–25 Hz) activity decreases were observed in association with behavioral tasks

(Mukamel et al. 2005; Tallon-Baudry et al. 2005; Crone et al. 2006; Miller et al. 2014; Herman et al. 2019; Li et al. 2019). In this study, we focused on investigating the broadband gamma activity due to its known correspondence to local population neuronal firing (Mukamel et al. 2005; Manning et al. 2009; Ray and Maunsell 2011) rather than event-related potentials (ERPs) or other low frequency signals, which are less well-localized and more susceptible to variations in the reference electrode location (Herman et al. 2019). Previously, time–frequency analysis of visual cortical responses due to letter events in the CPT task showed that the most prominent power changes compared to baseline can be observed within the 40–115 Hz frequency range (Li et al. 2019). Changes in gamma power were also observed in frequencies higher than 115 Hz; however, an upper cut-off of 115 Hz was selected to avoid powerline artifacts expected at 120 Hz, a harmonic of 60 Hz.

X-Press and NonX-NoPress trials were filtered using the `filtfilt` function in MATLAB 2019a to limit the frequency content of these trials within the broadband gamma frequency range (40–115 Hz) as performed previously (Li et al. 2019). After filtering, the first and last second of each 4-s epoch were removed to avoid filter edge effects. Therefore, the final epoch length was 2 s centered at stimulus onset. An analysis window size of 60 ms was chosen as a compromise to balance needs for sufficient temporal resolution on the one hand, and sufficient temporal smoothing for noise removal on the other. Gamma power was calculated by squaring the filtered signal and then averaging within 60-ms windows beginning with the first epoch sample, with 30 ms overlap across bins to smooth the power signals over time. Therefore, the gamma power binning procedure divided each 2-s epoch into a total of 65 windows, each lasting 60 ms. Trials with smoothed gamma power exceeding 20 SD of the mean power across trials for that electrode within each subject were excluded. The 7 windows (60 ms each, with 30 ms overlap) representing the time period from  $-240$  to  $0$  ms corresponded with the prestimulus or baseline period, while the 32 windows (again 60 ms each, with 30 ms overlap) encompassing  $0$  to  $1,000$  ms post-stimulus were considered as the neural response to the stimulus. The windows representing the time period from  $-1,000$  to  $-240$  ms were not considered as a part of the baseline period since they were contaminated by strong neural activity due to preceding stimuli. X-Press trials were z-scored using the mean and SD of the baseline gamma power across all X-Press trials. The same process was applied separately to z-scored NonX-NoPress trials. In particular, for each subject, the gamma power time course at each electrode of each X-Press or NonX-NoPress trial was z-score transformed using the mean and SD of the gamma power during the baseline period of that electrode across all corresponding X-Press or NonX-NoPress trials for that subject.

The z-scored X-Press and NonX-NoPress trials were considered for further examination that employed

combined trials (X-Press + NonX-NoPress) and difference of trials (X-Press – NonX-NoPress) analyses. For each subject, combined data were calculated at each electrode by averaging the z-scored gamma power time series across all X-Press and NonX-NoPress trials within that electrode regardless of the event type, whereas for difference of trials data, z-scored gamma power timeseries were first averaged within each event type for each electrode, and the difference of the electrode average z-scored gamma power was found between the X-Press and NonX-NoPress conditions.

### Mapping z-scored gamma power to standard Montreal Neurological Institute brain

A triangular mesh representing the standard Montreal Neurological Institute (MNI) cortical surface was created in BioImage Suite (<http://bioimagesuite.yale.edu/>) using the MNI Colin 22 brain template. BioImage Suite was used to determine electrode locations in MNI space based on each patient's pre-op MRI, post-op MRI, and post-op CT. Each electrode was assigned to the nearest vertex on the cortical surface. Z-scored gamma power values associated with each electrode were mapped to the standard MNI brain surface as described previously (Herman et al. 2019; Li et al. 2019). In particular, for each participant, all vertices within a 1 mm spherical radius from the central vertex to which that electrode was projected were assigned the same z-score values as the central vertex. A linear descending gradient function was used to assign gradually decreasing z-scored gamma values to vertices located within a 1–15 mm spherical radius from the central vertex where a z-score value of 0 was assigned to vertices at 15 mm from the central vertex. Within each subject, the z-score gamma power values associated with each vertex as a result of different electrodes contributing to that vertex were summed. To aggregate the z-scores of each vertex across subjects, a weighted average of these z-scores was obtained across subjects per each vertex by multiplying the average z-scores by the square root of the number of subjects contributing at each vertex location as previously described (Herman et al. 2019; Li et al. 2019).

### Statistical analyses

To identify the statistically significant changes in post-stimulus z-scored gamma power compared to the baseline, we employed a spatiotemporal cluster-based permutation test. This approach overcomes the multiple comparisons problem by implementing a single-test statistic for the entire spatiotemporal data grid instead of evaluating the statistical significance at each (vertex, time point) pair separately (Maris and Oostenveld 2007). To reduce dimensionality, the cortical surface mesh was converted to a bilateral parcellation map comprising 120 nonoverlapping regions (60 regions per hemisphere) (Fig. 1C) generated by applying K-means clustering to the 3-dimensional coordinates of the vertices such that

vertices within close proximity were clustered into the same parcel. We chose to use 120 parcels for the analysis to balance needs for sufficient spatial resolution on the one hand, and sufficient number of electrodes per parcel for statistical analysis on the other.

The cluster-based permutation statistical approach implemented was adapted from the Mass Univariate ERP Toolbox (Groppe et al. 2011) and applied separately to the combined trials (X-Press + NonX-NoPress) and difference of trials (X-Press – NonX-NoPress). Given that the cluster-based permutation test requires computing an adjacency matrix to identify the neighboring parcels, the test was run for each hemisphere separately. To obtain a cluster-based permutation distribution, the permuted values consisted of mean z-scored gamma power across electrodes within parcels and 60-ms time windows compared to the corresponding baseline values using a paired, 2-tailed t-test. For the X-Press + NonX-NoPress analysis, baseline was defined as the (non-zero) mean of the gamma power in the 240 ms prior to the stimulus, whereas for the X-Press – NonX-NoPress analysis, baseline was defined as zero, assuming no difference between trials on average prior to the stimulus (this was true in general; data not shown).

For each permutation, prior to calculating t-values, we first randomly shuffled the sign of gamma power values for each electrode to be positive or negative, effectively adding or subtracting it from baseline. This generated a set of t-values across parcels and 60-ms time windows. A parcel and time point were considered eligible to join a cluster based on spatiotemporal adjacency if the t-value fulfilled a set alpha threshold. Positive and negative clusters were defined separately using this threshold. Because the positive and negative values were randomly shuffled, we assumed the permutation distribution to be symmetrical, so to facilitate calculation we only retained negative clusters to create a one-sided distribution. Therefore, the alpha threshold was set at 0.025 (equivalent to 0.05 in a 2-sided distribution). Summed t-values for each spatiotemporal cluster were then computed by taking the sum of the t-values for all parcels and time points within each cluster. For each permutation, we retained only the negative cluster with the largest absolute t-value and collected these across 2,000 permutations to create a permutation distribution. To identify significant clusters in the unpermuted data, positive and negative clusters were identified separately, and summed t-values with absolute value above the outer 2.5% of the permutation distribution were considered significant (again equivalent to  $P < 0.05$  for a 2-sided distribution).

Since the K-means clustering algorithm uses a random seed to initialize the center of the parcels when creating the parcellation map, the algorithm does not converge to the exact same parcels in repeated runs and results in slightly different collections of vertices clustered together within each parcel. In other words,

the location of parcels varies slightly across runs of the algorithm. To ensure that the statistical testing was robust and invariant to the changes in parcel locations, we generated 100 separate parcellation maps by running K-means clustering 100 times and we ran the spatiotemporal cluster-based permutation test using each of the generated parcellation maps. This yielded 100 binary significance maps with a value of 1 at the location of significant parcels and a value of zero otherwise. To determine whether a vertex was significant, we used a majority vote approach across the 100 resultant significance maps; vertices that reached significance in more than 50% of the significance maps were considered significant. For both the combined trials (X-Press + NonX-NoPress) and difference of trials (X-Press—NonX-NoPress), we only displayed the z-scored gamma power for vertices that reached significance in more than 50% of the significance maps (see Figs. 2 and 3).

### Regions of interest

Eight anatomical regions of interest (ROIs) involved in the early stages of visual perception as well as task-specific neural changes were selected. The ROIs were obtained from the SPM12 toolbox (<https://www.fil.ion.ucl.ac.uk/spm/>) MarsBaR (voxel size =  $2 \times 2 \times 2$  mm) in MNI space (Tzourio-Mazoyer et al. 2002) and mapped onto the vertices of the brain surface mesh also in MNI space. The mapping was performed such that any vertex located within a maximum distance of 1.5 mm from the center of an ROI voxel was attributed to that ROI. However, some vertices on the mesh surface were not included in their corresponding ROIs and appeared as holes on the brain surface mesh because they did not fall within 1.5 mm from the center of MRI voxels especially at the depths of sulci and at the edges of ROIs so they needed to be corrected manually. Guided by visual inspection, the correction process was performed by changing the maximum allowed distance between the center of a voxel within an ROI and the nearest vertex on the brain mesh until all vertices were assigned appropriately to the correct nearest ROI.

ROIs (see Fig. 4A) included occipital cortex (O), fusiform gyrus (FG), parahippocampal gyrus (PH), caudal middle frontal gyrus (CMF), superior frontal gyrus (SF), parietal cortex (P), supplementary motor area (SMA), and precentral gyrus (PG). Calcarine, Cuneus, Lingual, Occipital\_Sup, Occipital\_Mid, Occipital\_Inf from MarsBaR were combined to form the occipital cortex (O) ROI. The parietal cortex (P) ROI was formed by grouping MarsBaR's Parietal\_Sup, Angular, Parietal\_Inf, and SupraMarginal ROIs. The caudal middle frontal gyrus (CMF) ROI is the caudal part of Frontal\_Mid from MarsBaR. Finally, FG, PH, SF, SMA, and PG ROIs correspond to Fusiform, Parahippocampal, Frontal\_Sup\_Medial, Supp\_Motor\_Area, and Precentral ROIs from MarsBaR, respectively.

For each ROI, average combined and difference time courses of the electrodes within that ROI were plotted separately for each hemisphere (see Fig. 4B and C).

For every subject, combined data were calculated at each electrode by averaging the z-scored gamma power timeseries across all X-Press and NonX-NoPress trials within that electrode regardless of the event type, whereas for difference data, z-scored gamma power timeseries were first averaged within each event type for each electrode, and the difference of the electrode average z-scored gamma power was found between the X-Press and NonX-NoPress conditions. For both combined and difference cases, the average across electrodes from all subjects was calculated and reported (Fig. 4B and C).

### Results

Two categories of trials, X-Press and NonX-NoPress, were analyzed for changes in z-score gamma power following visual letter stimuli presentation. Parallel analyses were applied to (i) combined trials (X-Press + NonX-NoPress) and (ii) difference of trials (X-Press—NonX-NoPress) to investigate the similarities and differences between the neural signals resulting from X-Press and NonX-NoPress events, especially at the early times post-stimulus that are hypothesized to be linked to the initial stages of visual signal detection leading to conscious perception. Cortical surface maps displaying gamma power changes are shown starting from the stimulus onset to 270 ms post-stimulus in 60 ms overlapping increments for combined and differences of trial types (Fig. 2). In Fig. 3, cortical surface maps of gamma power changes occurring at later time points from 300 to 990 ms post-stimulus are presented. ROIs and the corresponding gamma power time courses for combined and difference contrasts are shown in Fig. 4.

#### Early gamma power changes

Cluster-based permutation statistical analysis on the difference of trials revealed that there were no statistically significant changes between the gamma power responses within the first approximately 180 ms post-stimulus between X-Press and NonX-NoPress trial types (Fig. 2B). To increase statistical power, we combined the X-Press and NonX-NoPress trials to investigate the shared early changes across the 2 trial types (Fig. 2A).

For combined trials, cluster-based permutation statistical analysis on z-score gamma power changes revealed statistically significant bilateral increases in gamma power in the primary visual cortex, with an approximate onset from 30 to 90 ms post-stimulus (Fig. 2A). These changes co-occurred with increased bilateral gamma power in the caudal middle frontal gyrus (overlapping with the FEFs) and medial temporal PH, with the right PH slightly preceding the left. Sustained statistically significant early increases in gamma power were also found in the bilateral SF (Fig. 2A). At 30–90 ms post-stimulus, bilateral orbital frontal cortex and bilateral inferior frontal cortex showed significant gamma power increases (Fig. 2A). The right FG showed a prominent

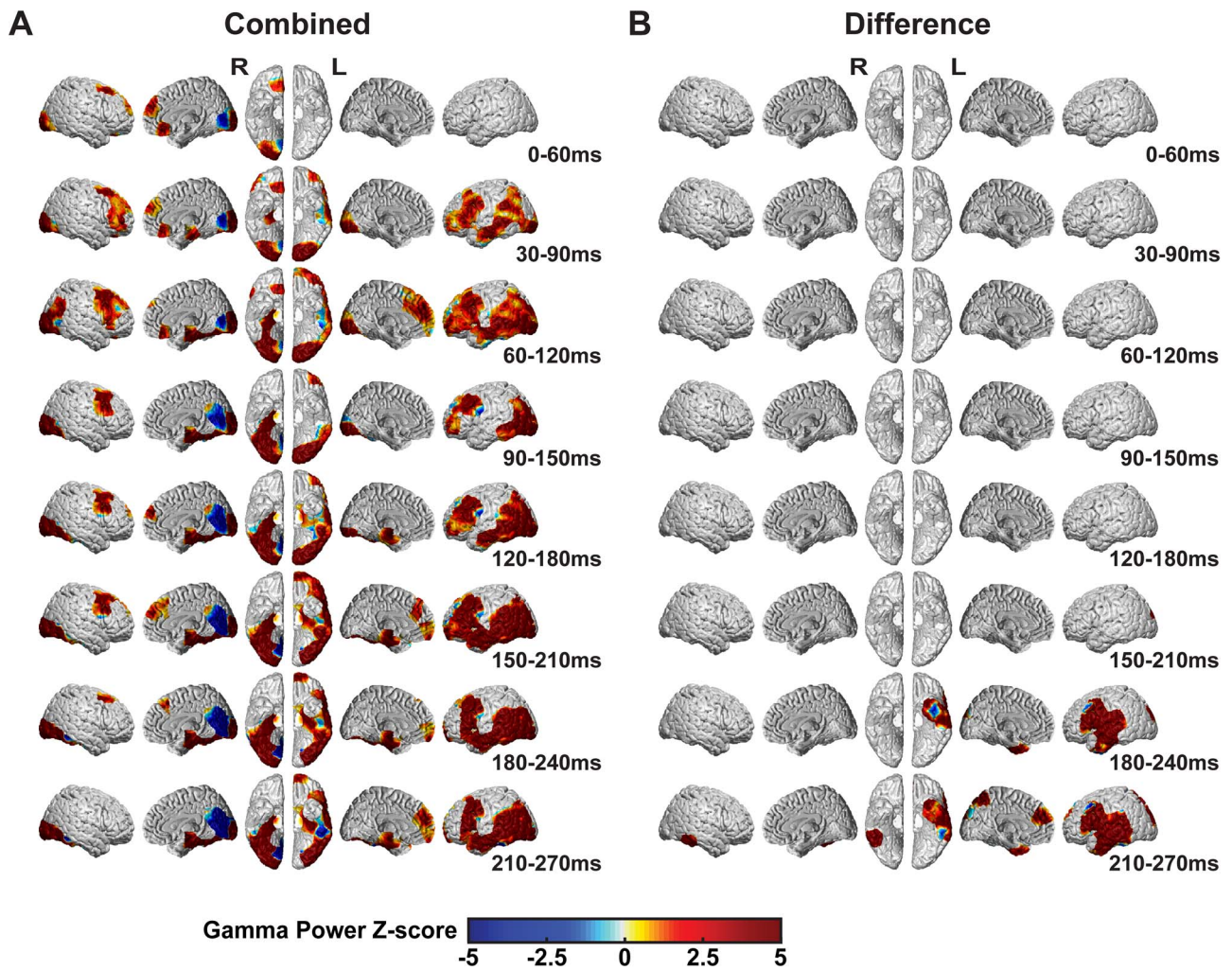


**Fig. 2.** Statistically significant gamma power changes at the early stages of visual conscious perception for combined (X-Press + NonX-NoPress) and difference (X-Press – NonX-NoPress) analyses of trial types ( $N = 10$  subjects). The significance was assessed using cluster-based permutation testing (see Materials and Methods) and only statistically significant changes are displayed. Displayed times are consecutive 60 ms analysis windows with 30 ms overlap. A) X-Press + NonX-NoPress: gamma power increases were observed at the earliest times after stimulus presentation (<180 ms) in bilateral visual cortex and FG, bilateral medial temporal PH, bilateral caudal middle frontal gyrus overlapping with FEF, bilateral SF, bilateral orbital frontal cortex, and bilateral inferior frontal cortex. Early increases were also observed in left lateral parietal cortex and left lateral temporal cortex. Decreases were observed in right anterior medial visual cortex (B) X-Press – NonX-NoPress: There were no significant gamma power differences at the earliest stage of stimulus presentation (<180 ms). At later times, differences emerged especially in left cortical areas (right hand was used for button press), seen more fully in Fig. 3.

gamma power increase at 60–120 ms post-stimulus, while a more gradual spread of increased gamma power across time was observed in the left FG. However, notably, our results regarding the full spatial extent of gamma power increases in the FG are limited by electrode coverage (Fig. 1B).

Even at these early time points, not all changes were observed bilaterally: an early sustained gamma power increase (30–360 ms; Figs. 2A and 3A) was observed across left superior and left inferior parietal lobules as well as left lateral temporal cortex. In contrast, early decreases were seen in right anterior medial occipital cortex overlapping with lingual gyrus, cuneus, and calcarine (Fig. 2A).

The ROI time courses for representative regions correspond with the early signal profiles from whole-brain

surface gamma power responses reported in Fig. 2. Combined time courses showed bilateral increased gamma power in the occipital cortex, fusiform, caudal middle frontal, and parahippocampal gyri within the first 180 ms post-stimulus onset (Fig. 4B). Early increases with smaller magnitudes were present bilaterally in superior frontal and parietal ROIs. Notably, the early changes in the abovementioned regions, except for the parietal ROI, were greater in magnitude in the right cortex compared to the left cortex (Fig. 4B). No early gamma power changes were observed in SMA or PG. As reported from the z-score gamma power maps (Fig. 2B), difference time courses showed limited signal changes at the early time points (Fig. 4C) in agreement with the lack of statistically significant changes at early times in Fig. 2B.

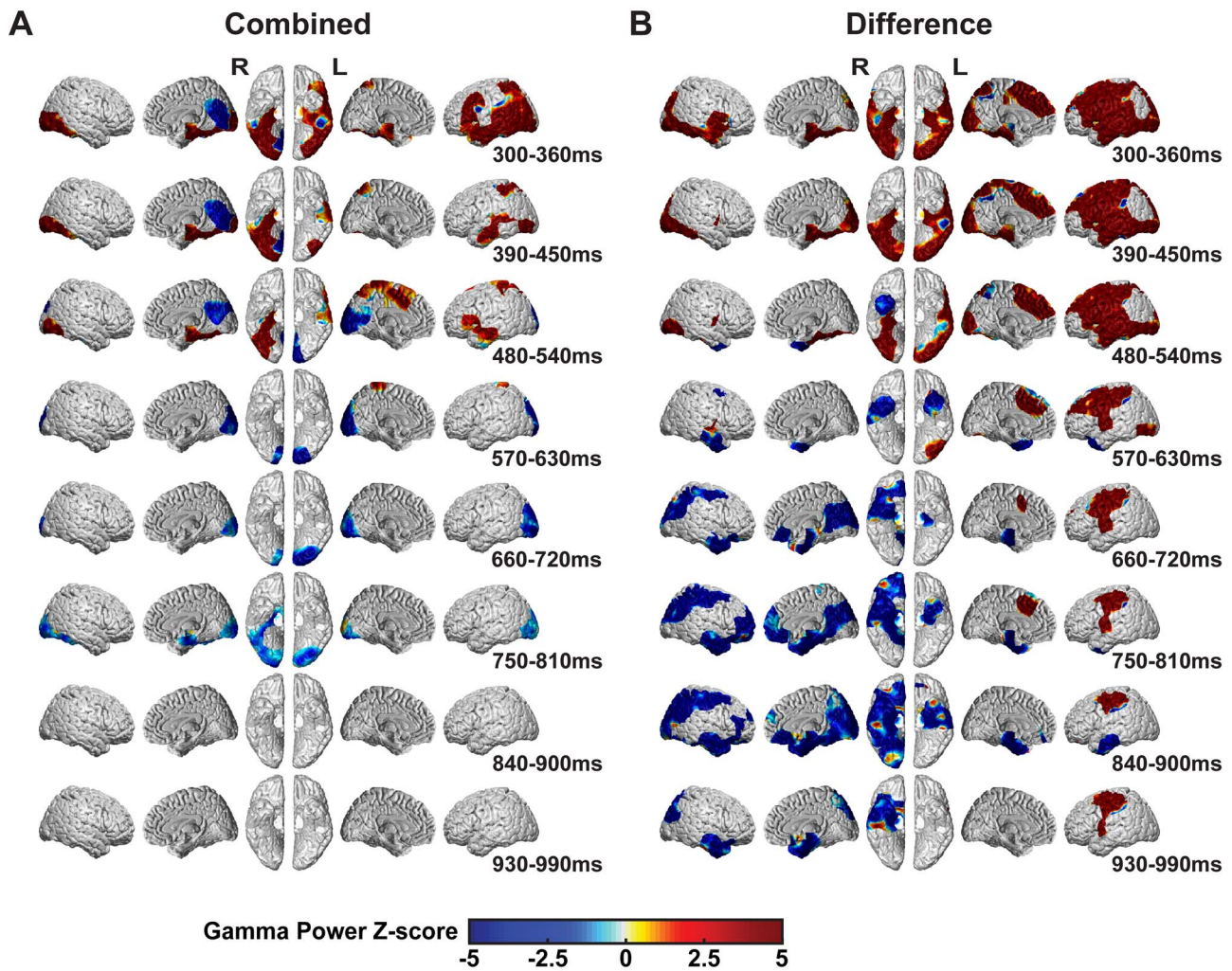


**Fig. 3.** Statistically significant gamma power changes at the late stages of visual conscious perception for combined (X-Press + NonX-NoPress) and difference (X-Press – NonX-NoPress) analyses of trial types ( $N = 10$  subjects). The significance was assessed using cluster-based permutation testing (see Methods) and only statistically significant changes are displayed. Analysis times were consecutive 60-ms analysis windows with 30 ms overlap as in Fig. 2, but some 60-ms windows were skipped here to allow display of the longer time periods. A) X-Press + NonX-NoPress: gamma power increases in the combined data were observed in various brain areas at later times ( $>300$  ms). This wave of increases receded at approximately 540 ms. B) X-Press – NonX-NoPress: gamma power associated with X-Press trials had greater magnitude in multiple regions of the left cortex. At later times, relatively decreased signal for X-Press trials was observed in the bilateral anterior/medial temporal cortex and in wide regions of the right hemisphere.

### Late gamma power changes

For the combined trials, cluster-based permutation statistical analysis revealed that the significant early gamma power changes observed at  $<180$  ms from stimulus onset increased in magnitude and spatial extent up to approximately 360 ms and then gradually diminished thereafter (Figs. 2A and 3A). However, considering the difference maps, the small statistically significant changes in gamma power observed at times  $>180$  ms continued to increase in magnitude and spatial extent at later timepoints (Figs. 2B and 3B). In particular, the difference maps showed that X-Press target trials showed greater gamma power in broad regions of the left hemisphere, which at later times coalesced into more focal sustained increases in the left PG (button press was with the right thumb, Fig. 3B). In addition, X-Press trials showed larger gamma power in the bilateral

medial temporal parahippocampal gyri at approximately 300–450 ms and lower gamma power in bilateral anterior temporal cortex as well as in broad regions of the right hemisphere at later times (Fig. 3B).

The ROI time courses displayed in Fig. 4 confirmed the late gamma power findings observed in the cortical surface maps for times  $>180$  ms post-stimulus. In particular, for combined trials, the initial gamma power increases observed in bilateral caudal middle frontal, superior frontal, parahippocampal, parietal, occipital, and fusiform cortex during the 250-ms visual stimuli faded towards zero in the period after stimulus offset (Fig. 4B). The difference analyses, on the other hand, showed delayed changes after stimulus offset in all regions, including greater left hemisphere gamma power for X-Press target trials in the left caudal middle frontal, superior frontal, parietal, occipital, fusiform,

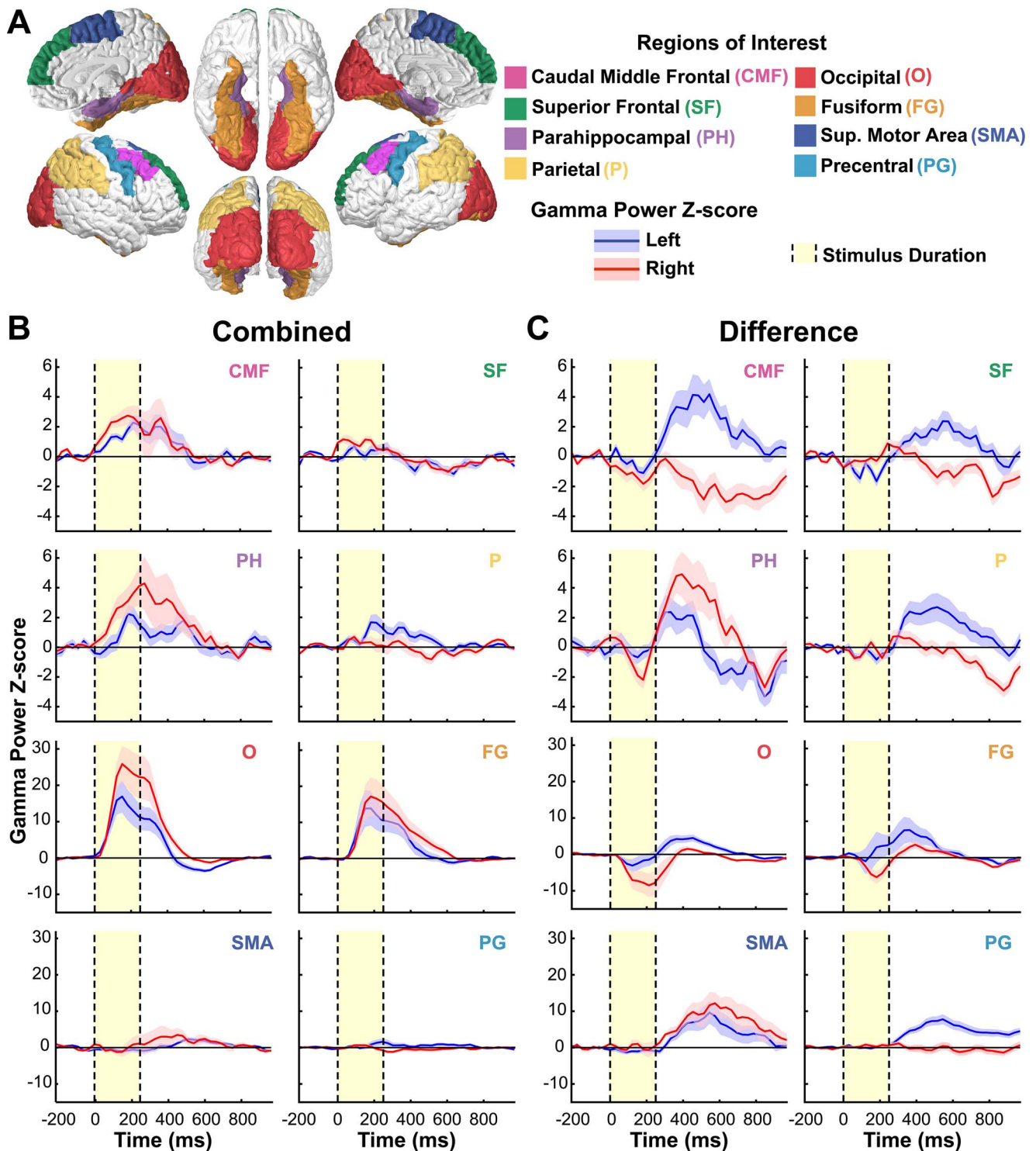


**Fig. 4.** Gamma power time courses of 8 anatomical ROIs. A) Eight representative anatomical ROIs were identified from the SPM12 toolbox MarsBaR (voxel size =  $2 \times 2 \times 2$  mm). The ROIs included caudal middle frontal gyrus (CMF), superior frontal gyrus (SF), parahippocampal gyrus (PH), parietal cortex (P), occipital cortex (O), fusiform gyrus (FG), supplementary motor area (SMA), and precentral gyrus (PG). B) X-Press + NonX-NoPress combined analyses: All ROIs except for SMA and PG showed early gamma power increases following the stimulus onset. C) X-Press - NonX-NoPress difference analyses: The most prominent gamma power differences were seen mainly at later times after stimulus presentation. Vertical black dashed lines and yellow shaded regions indicate timing of the 250-ms visual stimulus. Note difference in vertical scale in both B and C for the top 4 traces versus the bottom 4 traces. Same subjects and data as in Figs. 2 and 3.

and precentral cortex (traces above zero after stimulus offset in Fig. 4B), as well as initially greater and then lower power changes for X-Press target trials in bilateral parahippocampal cortex (biphasic traces after stimulus

offset in Fig. 4B), and lower power for X-Press target trials at later times in right hemisphere in caudal middle frontal, superior frontal, and parietal cortex (traces below zero after stimulus offset in Fig. 4B).

## Discussion

Using icEEG recordings, the current investigation aimed to study the gamma power changes associated with visual stimulus presentation and detection. Analyses focused on changes in gamma power at early and late periods post stimulus presentation. The CPT paradigm used fully opaque letters that were displayed for 250 ms. Because these stimuli should be fully visible for participants, the earliest changes were hypothesized to represent electrophysiological dynamics linked to conscious visual stimulus detection. The current results revealed a broad set of regions involved tens of milliseconds after stimulus presentation, comprising bilateral visual, prefrontal, medial temporal cortex, and left parietal and lateral temporal cortex. Meanwhile, at later times, sustained changes were observed overlapping the early response regions, but also recruiting more frontal, parietal, and temporal areas especially in the left hemisphere. These later responses may be linked to perceptual decision-making—a process in which sensory information is integrated and used to produce motor responses. Likewise, for X-Press events, when a button press was made after the presentation of the target stimulus, relatively larger gamma power increases were observed in left motor and premotor regions associated with right hand motor planning and execution, while relatively lower gamma power was observed in the right hemisphere.

### Early gamma power changes

At early times, no statistically significant gamma power differences were observed between target (X-Press) and nontarget (NonX-NoPress) events within 180 ms of stimulus onset (Figs. 2B and 4C). This suggested that the neural responses in the gamma range at the very early stages of visual perception are similar regardless of the event type, allowing these events to be combined for further investigation. At the earliest time points post-stimulus in combined analyses, cortical surface maps (Fig. 2A) and ROI time courses (Fig. 4B) showed bilateral gamma power increases in prefrontal cortex, particularly in the caudal middle frontal gyrus overlapping with FEF, orbital frontal cortex, and superior and inferior frontal cortex. The rapidity of these responses suggests that the dynamics in these first tens of milliseconds are involved in stimulus detection and sensory processing. Such findings are in line with previous human and nonhuman primate studies that suggest a major role for prefrontal cortex in the early stages of visual conscious perception within 100 ms from stimulus onset (Panagiotaropoulos et al. 2012). In both human and nonhuman primate studies, early activity was observed in the FEF within 100 ms post-stimulus characterized by increases in neural responses which correspond to visual perception and attention (Schmolsky et al. 1998; Blanke et al. 1999; Thompson and Schall 1999, 2000; Bichot and Schall 2002; Muggleton et al. 2003; O'Shea et al. 2004;

Gregoriou et al. 2009; Libedinsky and Livingstone 2011; Bollimunta et al. 2018). Other studies found that sensory information can reach FEF nearly as fast as the primary visual cortex in less than 50 ms, which is consistent with our findings (Kirchner et al. 2009; Kwon et al. 2021). Of note, we do not believe the early changes we observed are an artifact of the filtering and smoothing methods we used, because we found previously using the same approach with simulated data that temporal smearing (leakage) between time windows was minimal (Kwon et al. 2021).

In addition to the gamma power changes associated with FEF, early gamma power bilateral increases were observed in orbital frontal cortex and superior and inferior frontal cortex (Fig. 2A). A recent fMRI study reported that the inferior frontal gyrus is involved in stimulus detection (Weilhammer et al. 2021). The superior frontal and orbitofrontal areas are thought to contribute to higher cognitive functions (du Boisgueheneuc et al. 2006; Chaumon et al. 2014). Our findings suggest that these regions may also have a role in stimulus detection, and future work could investigate relationships between detection and higher cognitive functions in these brain areas.

Early gamma power increases were observed in bilateral occipital and bilateral fusiform gyri (Figs. 2A and 4B). These findings are consistent with previous human and nonhuman primate studies in visual stimulus detection (Schmolsky et al. 1998; Deco and Lee 2004; Meeren et al. 2008; Kirchner et al. 2009; Shigihara et al. 2016; Herman et al. 2019; Li et al. 2019; Kwon et al. 2021). However, the early decrease observed in right anterior medial occipital cortex is more challenging to interpret. Previous studies hypothesized that decreases in cortical gamma activity may suppress signaling that is irrelevant to task demands (Lachaux et al. 2008; Herman et al. 2019). Two previous icEEG studies from our research group found suppression of gamma power in visual cortex during active task phases of the CPT task and after stimulus perception in a visual awareness threshold task (Herman et al. 2019; Li et al. 2019). These and other previous findings led to the hypothesis that transient decreased visual cortex activity may be a mechanism to enhance signal-to-noise ratio through suppressing background neural activity and to improve performance in repetitive stimulus presentation tasks (Smith et al. 2000; Smith et al. 2004).

Our findings of medial temporal and medial frontal cortex involvement (Fig. 2A) are supported by a previous study, which found that both regions formed a stimulus detection network during visual search (Wang et al. 2018). Moreover, the involvement of the medial temporal cortex may reflect its role in higher-order stimulus processing and encoding (Hassabis et al. 2007; Schacter et al. 2007; Konkel and Cohen 2009).

Left inferior occipitotemporal cortex has been shown to be activated within 200 ms following presentation of written words and letter strings (Tarkiainen et al. 1999;

Vinckier et al. 2007). Our observation of even earlier involvement (Fig. 2A) suggests that activity in this region may not be limited to the processing of words, as such, but that it may have a critical role as part of an early visual detection network.

As hypothesized and anticipated by previous studies, we observed gamma power increases in the parietal cortex (Figs. 2A and 4B). Previous studies suggested that the parietal cortex plays an important role in visual perception and attention (Critchley 1962; Bisley and Goldberg 2010). Specifically, the parietal cortex provides top-down attentional feedback to sensory networks that can lead to modulation of neuronal activity relevant to the early stages of sensory signal processing (Corbetta and Shulman 2002; Saalmann et al. 2007; Gregoriou et al. 2009; Bisley and Goldberg 2010). The critical role of the parietal cortex attention network is supported by clinical data, which shows that damage of the parietal cortex can lead to spatial neglect (Parton et al. 2004).

It is important to compare and contrast the present results with another recent icEEG study we conducted of visual stimulus detection (Kwon et al. 2021). The present study used data from patients at Yale performing an attentional vigilance task (CPT), whereas the Kwon study used data from a different set of patients in a multi-site study performing the encoding phase of a visual word recall task. The present study found early increases in bilateral occipital, bilateral fusiform, bilateral frontal (including FEFs), bilateral medial temporal, and left lateral parietal-temporal cortex and decreases in right anterior medial occipital cortex. The Kwon study found early increases in bilateral occipital, bilateral fusiform, right frontal (including FEFs), and bilateral medial temporal cortex and decreases in left rostral middle frontal gyrus. Thus, although the tasks and other conditions were different in the 2 studies, both showed early increases in bilateral occipital, bilateral fusiform, right frontal (including FEFs), and bilateral medial temporal cortex, implying that the visual detection signals in these regions are robust and task-independent. Differences between the 2 studies, possibly related to different tasks or other factors, can be summarized as follows: (i) only the present study showed increases in left frontal (including FEFs) and left lateral parietal-temporal cortex and decreases in right anterior medial occipital cortex; (ii) only the Kwon study showed decreases in left rostral middle frontal gyrus. In summary, the combined results of these 2 studies suggest that there may be a core network of cortical regions involved in early visual stimulus detection for these 2 different tasks, consisting of bilateral occipital, bilateral fusiform, right frontal (including FEF), and bilateral medial temporal cortex.

### Late gamma power changes

The gamma power increases observed in prefrontal, parietal, medial, and lateral temporal regions at the

early stages after stimulus presentation persisted into late time periods (>180 ms) (Figs. 2A and 3A), suggesting that these regions may play important roles in both detection and higher-order processing, such as perceptual decision-making (Hauser and Salinas 2014). Numerous studies have identified frontoparietal networks involved in the perceptual decision-making process (Kable and Glimcher 2009; Li et al. 2009; Siegel et al. 2011; Mulder et al. 2012; Keuken et al. 2014; Yeon et al. 2020). In line with our findings (Figs. 2A and 3A), frontal areas of perceptual decision-making networks reported in the literature included inferior frontal gyrus, middle frontal gyrus, superior frontal, and orbitofrontal cortex. Our observed gamma power increases in the parietal cortex align with studies that reported intraparietal sulcus and inferior parietal lobule as a part of a frontoparietal detection network. Indeed, activity within the lateral intraparietal cortex has been shown to reflect accumulation of sensory evidence prior to response (Shadlen and Newsome 2001). The changes observed in the anterior cingulate cortex (ACC) (Fig. 2A) correspond with prior studies, suggesting that the ACC may be involved in guiding decision-making and providing the appropriate target-specific response (Thielscher and Pessoa 2007; Scheibe et al. 2010; Yeon et al. 2020).

Widespread gamma power differences were observed in the left hemisphere for X-Press versus NonX-NoPress events between 300 and 540 ms in frontal, parietal and temporal areas (Fig. 3B). These differences receded later leaving a persistent gamma power difference in SMA and left PG responsible for right hand motor planning and execution. Interestingly, prior work has shown more spatially restricted changes associated with target detection and decision-making in nonhuman primates (Chelazzi et al. 2001; Reynolds and Chelazzi 2004; Bichot et al. 2005), and human studies identified localized regions that mediate discrimination of targets including inferior occipital gyrus, inferior temporal gyrus, FG, superior parietal gyrus, middle frontal gyrus, supramarginal gyrus as well as medial frontal cortex (Peelena and Kastner 2011; Bansal et al. 2014; Wang et al. 2018). These regions are in line with our findings at earlier times; however, the activity observed in our study starting at 330 ms is less spatially circumscribed compared to these studies. This could be attributed to the differences in recording techniques, the analyzed frequency ranges, electrode coverage in the intracranial studies as well as differences in the tasks presented to the participants. The gamma power increases associated with X-Press events in PG are in line with prior work by Muthukumaraswamy (2010). Frontal, parietal, and temporal regions within the right cortex showed a sustained gamma power negative difference with a relative decrease for X-Press target trials (Fig. 3B). The right cortex negative differences are in line with prior studies suggesting a right hemisphere dominance for response inhibition (Swick et al. 2011; Coxon et al. 2016).

## Conclusions and future directions

Here we identified a network of early neural activity increases in bilateral occipital, fusiform, frontal and medial temporal cortices, left lateral parietal-temporal cortex and decreases in right anterior medial occipital cortex all within 30–180 ms of stimulus onset in a visual attentional vigilance task. Given the clear visibility of high contrast stimuli presented in the center of the visual field, and very high proportion of correct responses both to target and nontarget stimuli, it is reasonable to assume that nearly all stimuli were consciously perceived by the participants; although it is important to acknowledge that consciousness was not explicitly tested in the present study. Other recent work directly testing conscious visual perception has shown a similar detection network in bilateral visual cortex, FG, and posterior middle frontal gyrus/FEFs using fMRI, albeit at much lower temporal resolution (Kronemer et al. 2021). These findings and other recent studies suggest that an early stimulus detection network is the first step in conscious visual perception, initiating other subsequent cortical and subcortical mechanisms overlapping in space and time (Blumenfeld 2021).

The present work should be extended through additional future studies. One limitation of the current investigation is the limited number of participants combined with the nonuniformity of the electrode density, which yielded a small number of electrodes in some regions of the brain especially the medial surface. Important changes, especially in the default mode network, could be better investigated with more extensive coverage in these regions. With a larger sample size, future investigations could also address whether there is a relation between response times and the variations in gamma power magnitude (or power in other frequency ranges) post stimulus. In addition, study of different behavioral paradigms with larger error rates than the present study could investigate relationships between early neural signals and the accuracy of participant responses. Future investigations should also compare the detection of different stimuli across different sensory modalities to determine if each sensory system or stimulus type involves detection networks with unique spatiotemporal characteristics. Moreover, recruiting patients with subcortical depth electrodes could produce a powerful dataset to find subcortical contributions along with the cortical network described in this study. These additional studies will help to advance the investigation of the neural mechanism of detection, further elucidating the earliest stages of sensory processing and contributions to later perception and behavior.

## Funding

This work was supported by the Betsy and Jonathan Blattmachr Family and by the Mark Loughridge and Michele Williams Foundation.

*Conflict of interest statement.* None declared.

## References

- Bansal AK, Madhavan R, Agam Y, Golby A, Madsen JR, Kreiman G. Neural dynamics underlying target detection in the human brain. *J Neurosci*. 2014;34(8):3042–3055.
- Beck LH, Bransome ED Jr, Mirsky AF, Rosvold HE, Sarason I. A continuous performance test of brain damage. *J Consult Psychol*. 1956;20(5):343–350.
- Bichot NP, Schall JD. Priming in macaque frontal cortex during popout visual search: feature-based facilitation and location-based inhibition of return. *J Neurosci*. 2002;22(11):4675–4685.
- Bichot NP, Rossi AF, Desimone R. Parallel and serial neural mechanisms for visual search in macaque area V4. *Science*. 2005;308(5721):529–534.
- Bisley JW, Goldberg ME. Attention, intention, and priority in the parietal lobe. *Annu Rev Neurosci*. 2010;33(1):1–21.
- Blanke O, Morand S, Thut G, Michel CM, Spinelli L, Landis T, Seeck M. Visual activity in the human frontal eye field. *Neuroreport*. 1999;10(5):925–930.
- Blumenfeld H. Brain mechanisms of conscious awareness: detect, pulse, switch, and wave. *Neuroscientist*. 2021. <https://doi.org/10.1177/10738584211049378>.
- du Boisgueheneuc F, Levy R, Volle E, Seassau M, Duffau H, Kinkingnehun S, Samson Y, Zhang S, Dubois B. Functions of the left superior frontal gyrus in humans: a lesion study. *Brain*. 2006;129(Pt 12):3315–3328.
- Bollimunta A, Bogadhi AR, Krauzlis RJ. Comparing frontal eye field and superior colliculus contributions to covert spatial attention. *Nat Commun*. 2018;9(1):3553.
- Chaumon M, Kveraga K, Barrett LF, Bar M. Visual predictions in the orbitofrontal cortex rely on associative content. *Cereb Cortex*. 2014;24(11):2899–2907.
- Chelazzi L, Miller EK, Duncan J, Desimone R. Responses of neurons in macaque area V4 during memory-guided visual search. *Cereb Cortex*. 2001;11(8):761–772.
- Corbetta M, Shulman GL. Control of goal-directed and stimulus-driven attention in the brain. *Nat Rev Neurosci*. 2002;3(3):201–215.
- Coxon JP, Goble DJ, Leunissen I, Van Impe A, Wenderoth N, Swinnen SP. Functional brain activation associated with inhibitory control deficits in older adults. *Cereb Cortex*. 2016;26(1):12–22.
- Critchley M. Clinical investigation of disease of the parietal lobes of the brain. *Med Clin North Am*. 1962;46(3):837–857.
- Crone NE, Sinai A, Korzeniewska A. High-frequency gamma oscillations and human brain mapping with electrocorticography. *Prog Brain Res*. 2006;159:275–295.
- Deco G, Lee TS. The role of early visual cortex in visual integration: a neural model of recurrent interaction. *Eur J Neurosci*. 2004;20(4):1089–1100.
- Foxe JJ, Simpson GV. Flow of activation from V1 to frontal cortex in humans - a framework for defining "early" visual processing. *Exp Brain Res*. 2002;142(1):139–150.
- Gregoriou GG, Gotts SJ, Zhou HH, Desimone R. High-frequency, long-range coupling between prefrontal and visual cortex during attention. *Science*. 2009;324(5931):1207–1210.
- Groppe DM, Urbach TP, Kutas M. Mass univariate analysis of event-related brain potentials/fields I: a critical tutorial review. *Psychophysiology*. 2011;48(12):1711–1725.
- Hassabis D, Kumaran D, Vann SD, Maguire EA. Patients with hippocampal amnesia cannot imagine new experiences. *Proc Natl Acad Sci U S A*. 2007;104(5):1726–1731.
- Hauser CK, Salinas E. Perceptual decision making. In: *Encyclopedia of computational neuroscience*; NY: Springer, 2014. pp. 1–21

- Herman WX, Smith RE, Kronemer SI, Watsky RE, Chen WC, Gober LM, Touloumes GJ, Khosla M, Raja A, Horien CL, et al. A switch and wave of neuronal activity in the cerebral cortex during the first second of conscious perception. *Cereb Cortex*. 2019;29(2):461–474.
- Kable JW, Glimcher PW. The neurobiology of decision: consensus and controversy. *Neuron*. 2009;63(6):733–745.
- Keuken MC, Muller-Axt C, Langner R, Eickhoff SB, Forstmann BU, Neumann J. Brain networks of perceptual decision-making: an fMRI ALE meta-analysis. *Front Hum Neurosci*. 2014;8:445.
- Killory BD, Bai X, Negishi M, Vega C, Spann MN, Vestal M, Guo J, Berman R, Danielson N, Trejo J, et al. Impaired attention and network connectivity in childhood absence epilepsy. *NeuroImage*. 2011;56(4):2209–2217.
- Kirchner H, Barbeau EJ, Thorpe SJ, Regis J, Liegeois-Chauvel C. Ultra-rapid sensory responses in the human frontal eye field region. *J Neurosci*. 2009;29(23):7599–7606.
- Konkel A, Cohen NJ. Relational memory and the hippocampus: representations and methods. *Front Neurosci*. 2009;3(2):166–174.
- Kronemer SI, Aksen M, Ding J, Ryu JH, Xin Q, Ding Z, Prince JS, Kwon H, Khalaf A, Forman S, et al. Brain networks in human conscious visual perception. *bioRxiv*. 2021. <https://doi.org/10.1101/2021.10.04.462661v1>.
- Kwon H, Kronemer SI, Christison-Lagay KL, Khalaf A, Li J, Ding JZ, Freedman NC, Blumenfeld H. Early cortical signals in visual stimulus detection. *NeuroImage*. 2021;244:118608.
- Lachaux JP, Jung J, Mainy N, Dreher JC, Bertrand O, Baciou M, Minotti L, Hoffmann D, Kahane P. Silence is golden: transient neural deactivation in the prefrontal cortex during attentive reading. *Cereb Cortex*. 2008;18(2):443–450.
- Li S, Mayhew SD, Kourtzi Z. Learning shapes the representation of behavioral choice in the human brain. *Neuron*. 2009;62(3):441–452.
- Li J, Kronemer SI, Herman WX, Kwon H, Ryu JH, Micek C, Wu Y, Gerrard J, Spencer DD, Blumenfeld H. Default mode and visual network activity in an attention task: direct measurement with intracranial EEG. *NeuroImage*. 2019;201:116003.
- Libedinsky C, Livingstone M. Role of prefrontal cortex in conscious visual perception. *J Neurosci*. 2011;31(1):64–69.
- Manning JR, Jacobs J, Fried I, Kahana MJ. Broadband shifts in local field potential power spectra are correlated with single-neuron spiking in humans. *J Neurosci*. 2009;29(43):13613–13620.
- Maris E, Oostenveld R. Nonparametric statistical testing of EEG- and MEG-data. *J Neurosci Methods*. 2007;164(1):177–190.
- Meeren HKM, Hadjikhani N, Ahlfors SP, Hamalainen MS, de Gelder B. Early category-specific cortical activation revealed by visual stimulus inversion. *PLoS One*. 2008;3(10):e3503.
- Miller KJ, Honey CJ, Hermes D, Rao RP, denNijs M, Ojemann JG. Broadband changes in the cortical surface potential track activation of functionally diverse neuronal populations. *NeuroImage*. 2014;85(Pt 2):711–720.
- Muggleton NG, Juan CH, Cowey A, Walsh V. Human frontal eye fields and visual search. *J Neurophysiol*. 2003;89(6):3340–3343.
- Mukamel R, Gelbard H, Arieli A, Hasson U, Fried I, Malach R. Coupling between neuronal firing, field potentials, and fMRI in human auditory cortex. *Science*. 2005;309(5736):951–954.
- Mulder MJ, Wagenmakers EJ, Ratcliff R, Boekel W, Forstmann BU. Bias in the brain: a diffusion model analysis of prior probability and potential payoff. *J Neurosci*. 2012;32(7):2335–2343.
- Muthukumaraswamy SD. Functional properties of human primary motor cortex gamma oscillations. *J Neurophysiol*. 2010;104(5):2873–2885.
- O'Shea J, Muggleton NG, Cowey A, Walsh V. Timing of target discrimination in human frontal eye fields. *J Cogn Neurosci*. 2004;16(6):1060–1067.
- Panagiotaropoulos TI, Deco G, Kapoor V, Logothetis NK. Neuronal discharges and gamma oscillations explicitly reflect visual consciousness in the lateral prefrontal cortex. *Neuron*. 2012;74(5):924–935.
- Parton A, Malhotra P, Husain M. Hemispatial neglect. *J Neurol Neurosurg Psychiatry*. 2004;75(1):13–21.
- Parvizi J, Kastner S. Promises and limitations of human intracranial electroencephalography. *Nat Neurosci*. 2018;21(4):474–483.
- Peelena MV, Kastner S. A neural basis for real-world visual search in human occipitotemporal cortex. *Proc Natl Acad Sci U S A*. 2011;108(29):12125–12130.
- Ray S, Maunsell JH. Different origins of gamma rhythm and high-gamma activity in macaque visual cortex. *PLoS Biol*. 2011;9(4):e1000610.
- Reynolds JH, Chelazzi L. Attentional modulation of visual processing. *Annu Rev Neurosci*. 2004;27(1):611–647.
- Riccio CA, Reynolds CR, Lowe P, Moore JJ. The continuous performance test: a window on the neural substrates for attention? *Arch Clin Neuropsychol*. 2002;17(3):235–272.
- Saalmann YB, Pigarev IN, Vidyasagar TR. Neural mechanisms of visual attention: how top-down feedback highlights relevant locations. *Science*. 2007;316(5831):1612–1615.
- Schacter DL, Addis DR, Buckner RL. Remembering the past to imagine the future: the prospective brain. *Nat Rev Neurosci*. 2007;8(9):657–661.
- Scheibe C, Ullsperger M, Sommer W, Heekeren HR. Effects of parametrical and trial-to-trial variation in prior probability processing revealed by simultaneous electroencephalogram/functional magnetic resonance imaging. *J Neurosci*. 2010;30(49):16709–16717.
- Schmolsky MT, Wang Y, Hanes DP, Thompson KG, Leutgeb S, Schall JD, Leventhal AG. Signal timing across the macaque visual system. *J Neurophysiol*. 1998;79(6):3272–3278.
- Shadlen MN, Newsome WT. Neural basis of a perceptual decision in the parietal cortex (area LIP) of the rhesus monkey. *J Neurophysiol*. 2001;86(4):1916–1936.
- Shigihara Y, Hoshi H, Zeki S. Early visual cortical responses produced by checkerboard pattern stimulation. *NeuroImage*. 2016;134:532–539.
- Siegel M, Engel AK, Donner TH. Cortical network dynamics of perceptual decision-making in the human brain. *Front Hum Neurosci*. 2011;5:21.
- Smith AT, Singh KD, Greenlee MW. Attentional suppression of activity in the human visual cortex. *Neuroreport*. 2000;11(2):271–277.
- Smith AT, Williams AL, Singh KD. Negative BOLD in the visual cortex: Evidence against blood stealing. *Hum Brain Mapp*. 2004;21(4):213–220.
- Swick D, Ashley V, Turken U. Are the neural correlates of stopping and not going identical? Quantitative meta-analysis of two response inhibition tasks. *NeuroImage*. 2011;56(3):1655–1665.
- Tallon-Baudry C, Bertrand O, Henaff MA, Isnard J, Fischer C. Attention modulates gamma-band oscillations differently in the human lateral occipital cortex and fusiform gyrus. *Cereb Cortex*. 2005;15(5):654–662.
- Tarkiainen A, Helenius P, Hansen PC, Cornelissen PL, Salmelin R. Dynamics of letter string perception in the human occipitotemporal cortex. *Brain*. 1999;122(Pt 11):2119–2132.
- Thielscher A, Pessoa L. Neural correlates of perceptual choice and decision making during fear-disgust discrimination. *J Neurosci*. 2007;27(11):2908–2917.

- Thompson KG, Schall JD. The detection of visual signals by macaque frontal eye field during masking. *Nat Neurosci.* 1999;2(3):283–288.
- Thompson KG, Schall JD. Antecedents and correlates of visual detection and awareness in macaque prefrontal cortex. *Vis Res.* 2000;40(10-12):1523–1538.
- Tzourio-Mazoyer N, Landeau B, Papathanassiou D, Crivello F, Etard O, Delcroix N, Mazoyer B, Joliot M. Automated anatomical labeling of activations in SPM using a macroscopic anatomical parcellation of the MNI MRI single-subject brain. *NeuroImage.* 2002;15(1):273–289.
- Vinckier F, Dehaene S, Jobert A, Dubus JP, Sigman M, Cohen L. Hierarchical coding of letter strings in the ventral stream: dissecting the inner organization of the visual word-form system. *Neuron.* 2007;55(1):143–156.
- Wang S, Mamelak AN, Adolphs R, Rutishauser U. Encoding of target detection during visual search by single neurons in the human brain. *Curr Biol.* 2018;28(13):2058–2069.e4.
- Weilnhammer V, Fritsch M, Chikermane M, Eckert AL, Kanthak K, Stuke H, Kaminski J, Sterzer P. An active role of inferior frontal cortex in conscious experience. *Curr Biol.* 2021;31(13):2868–2880.e8.
- Yeon J, Shekhar M, Rahnev D. Overlapping and unique neural circuits are activated during perceptual decision making and confidence. *Sci Rep.* 2020;10(1):20761.